Sub Topic: Diagnostics

12th U.S. National Combustion Meeting
Organized by the Central States Section of the Combustion Institute
May 24–26, 2021 (Virtual)
College Station, Texas

Flame-drift velocimetry and flame morphology measurements with dual-perspective imaging in a shock tube

Adam J. Susa[1,*] *and Ronald K. Hanson*[1]

[1]*Mechanical Engineering, Stanford University, Stanford, CA, United States*
[*]*Corresponding author:* asusa@stanford.edu

Abstract: The application of simultaneous, dual-perspective, high-speed imaging to expanding flame experiments in a shock tube provides new opportunities to characterize the post-reflected-shock flow field. The shock-tube flame speed method has recently been demonstrated as an experimental approach to enable flame speed measurements at high unburned-gas temperatures inaccessible to previously established methodologies. The fidelity of these experiments are predicated on two underlying assumptions: quiescence of the unburned gas and symmetry of the expanding flames. While both are ubiquitous in the related literature, neither of these assumptions had been previously explicitly evaluated in relation to shock-tube flame experiments. This work reports the first measurements in which side-wall emission imaging, in addition to simultaneous end-wall imaging, is applied to expanding flame experiments in a shock tube. The fact that the burned gas within an expanding flame is nominally stagnant relative to the local flow field is leveraged to perform single-point, 3D velocimetry measurements of the core gas based upon the motion of the flame centroid, or "flame drift". These measurements reveal that minimal motion is present in the radial directions, while the velocity of the core gas in the axial direction is larger in magnitude and displays strong temperature dependence. The 3D morphology of flames is also characterized for the first time. Side wall imaging reveals that, while the expected flame symmetry is observed under some conditions, it breaks down under others, particularly at increasing temperatures. These results shed new light on previously reported flame structure observed in shock-tube flame experiments, which can now be explained as the axial integration of emission from an axially distorted flame. These observations serve as a demonstration of a novel diagnostic application, provide new insight as to how future shock-tube flame experiments might be refined, and motivate the continued use of side-wall imaging to ensure the fidelity of future shock-tube flame speed measurements.
Keywords: ***Shock tube, Imaging, Velocimetry, Laminar flames***

1. Introduction

The shock tube has been long regarded as a preferred, zero-dimensional apparatus for the study of chemical kinetics at high temperatures [1–4]. Nevertheless, it was not until the recent work of Ferris et al. that the potential of shock tubes to enable the study of laminar flames at high unburned-gas temperatures (T_u), conditions not otherwise accessible to experimental investigation, was first recognized [5]. Shock tubes can readily produce post-reflected-shock (region-5) temperatures in the range 400 K $< T_5 <$ 5,000+ K and pressures (P_5) from sub-atmospheric to 100s of atmospheres. Heating of the unburned test gas can be achieved on microsecond timescales by successive passage of the incident and reflected shock waves, timescales much shorter than that of spontaneous combustion chemistry over a wide range of engine-relevant conditions at which fundamental studies of flame dynamics were not previously possible but would be of tremendous value.

Two key assumptions have underlaid investigations performed with the shock-tube flame speed method reported to date; unburned gas quiescence and flame symmetry. As the driven-side end wall of the shock tube represents an impermeable boundary subject to a no-slip boundary condition, stagnation of the gas at the end wall is expected to hold exactly and is foundational to solution methods for the shock-jump equations [e.g. 6], but may break down away from the end wall due to non-ideal boundary layer effects [7]. Similarly, plasma kernels generated through laser-induced breakdown, their associated toroidal flow fields, and flames ignited from such plasmas are all commonly considered as being axis-symmetric about the path of the igniting beam [e.g. 8–11]. Applied to shock-tube flame experiments, this assumption formed a basis for the aspherical correction reported by Ferris et al. [5] and was implicit in the multi-stage flame structure hypothesized as a possible explanation for the structure observed in high-temperature *n*-heptane and *iso*-octane flames [12, 13], observations for which the present work provides a revised understanding.

In this work, simultaneous side- and end-wall emission imaging is applied to shock tube flame experiments for the first time, providing enhanced characterization of the post-reflected-shock environment and morphology of flames ignited within it. Gas velocity measurements behind the reflected shock are performed by monitoring the motion of early-stage flame kernels, in a method referred to here as flame-drift velocimetry (FDV). As a seedless, single-point velocimetry technique, FDV is similar to the laser-induced plasma image velocimetry (LIPIV) described by Shi et al. [14, 15]. However, by using the laser-induced plasma to ignite a flame producing sustained chemiluminescence, FDV can provide measurements over a longer time window than LIPIV measurements, which must be completed during the short emission lifetime of the plasma. Axial velocity measurements obtained using the FDV method are compared across wide ranges of conditions and tied to the physical phenomena of shock attenuation and post-reflected-shock pressure change ($\mathrm{d}P_5/\mathrm{d}t$). Separately, qualitative evaluation of the side-wall emission images provides new insight into the morphology of flames in the shock-tube environment, demonstrating regimes of both the expected symmetry and of axial distortion, the latter of which provides a likely explanation for previously reported flame structure [12, 13].

2. Experimental Methods

2.1 Experimental Setup

Experiments reported in this work are performed in a stainless-steel, 11.5-cm-diameter, extended-test-time shock tube, described in detail by Campbell et al. [6]. A Kister pressure transducer located 2 cm from the driven end wall provides high-speed pressure measurements throughout the experiment. Fast-response, PCB pressure transducers at four locations along the length of the tube record the step changes in pressure associated with the passage of the shock waves. All pressure signals are recorded at 10 MHz by a PXI-6115 multifunction data acquisition system; by logging the complete time-resolved pressure traces, the timing and speeds of both the incident and reflected shocks can be obtained from the PCB data (Sec. 2.2).

A dual-camera imaging configuration was devised to provide simultaneous side-wall and end-wall imaging of flames in the shock tube, as diagrammed in Fig. 1. A quartz end-wall window provides axial optical access to the shock tube [16]. End-wall emission images are recorded by a Phantom v2012 camera (Vision Research) with an ultraviolet- (UV-) sensitive, high-speed intensified relay optic (HS-IRO-X, LaVision); images are recorded through a 200-mm-focal-length, f/4

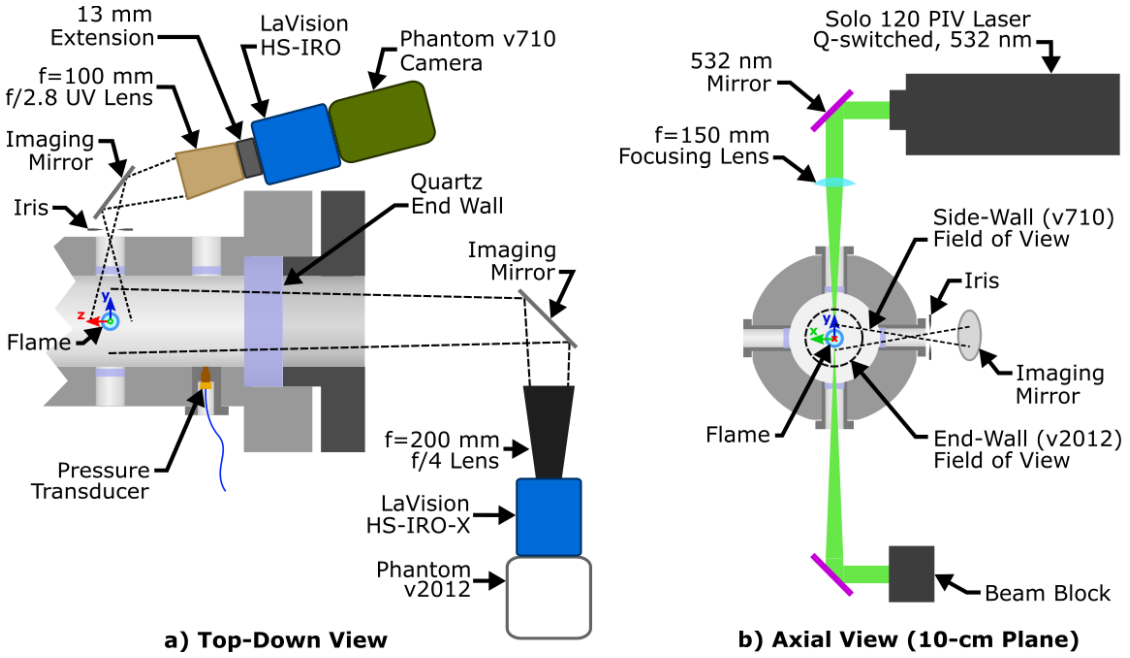

Figure 1: Schematic of the instrumentation used in this work, as viewed a) from the top and b) from the end of the tube. The shock tube is shown in cross section. The ignition laser in (a) and cameras in (b) are out of plane and not shown for clarity. Schematic not to scale; imaging ray tracing is approximate.

Nikkor lens. This configuration provides a 7-cm field of view (FOV) at 124 pixel-per-cm resolution on a 800-by-896-pixel image sensor region recorded at 20,000 frames per second (fps).

The 1.8-cm-diameter side-wall port, being the only side-wall optical access, presented an imaging challenge. In order to maximize the FOV at the center of the shock tube, a large, f/2.8-aperture lens is used, offset by a 13-mm extension ring to produce a converging, hypercentric arrangement. An iris is positioned just outside the optical plug to restrict the collection angle of light and flatten the spatial intensity profile observed at the in-shock-tube focal plane. With this arrangement, and the intensification provided by a HS-IRO (LaVision) to compensate for the low collection efficiency of emitted light, a roughly 2.5-cm FOV is realized. Images are recorded using a reduced, 528-by-520-pixel sensor region of a Phantom v710 camera (Vision Research) at 191 pixel-per-cm resolution and 20,000 fps to match the frame rate of the end-wall recordings.

In the shock-tube flame speed method, flames are initiated behind reflected shock waves by a plasma spark generated through laser-induced breakdown [5]. A flash-lamp-pumped, q-switched, neodymium-doped yttrium aluminum garnet (Nd:YAG) laser (Solo PIV 120, New Wave Research) is used as the ignition-laser source. The laser is internally frequency doubled to 532 nm and produces quoted pulse lengths of 3-5 ns. The maximum pulse energy is 120 mJ; in practice the energy is reduced by intentionally detuning the q-switch delay time relative to the flash lamp. The spark timing after the reflected-shock passage (t_{spark}) is precisely and flexibly controlled through external triggering of the laser by an upstream PCB pressure transducer. The beam is focused by a 15-cm-focal-length, best-form spherical lens before passing into the shock tube, creating a focused beam waist at the center of the tube where laser-induced breakdown occurs and the flame is ignited.

2.2 Velocimetry Data Interpretation

The extraction of velocities from the emission videos is a straightforward endeavor. Images are binarized using an Otsu threshold method [17] and the binary images are cleaned using morphological closing and filling operations [18, 19]. The centroid of the binary region representing the flame is extracted and the displacement of the centroid in each frame is calculated relative to the first frame. End-wall images provide X-Y centroid positions, while side-wall images provide Y-Z locations (see Fig. 1). The average velocity over an interval is taken as the slope of the centroid position vs. time data, shown in Fig. 2 for the first six frames following the spark, spanning a period of 250 μs; this same time interval was used for all measurements reported in this work.

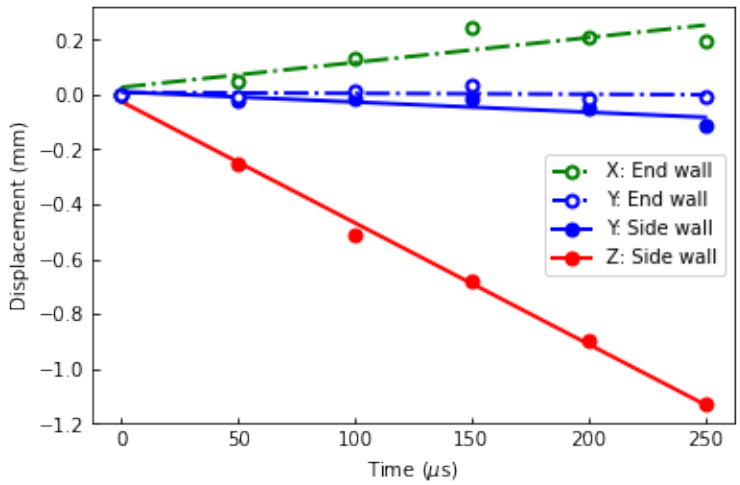

Figure 2: Flame-drift displacements and linear velocity fits from a lean ($\phi = 0.5$) *n*-heptane/O_2/Ar experiment with $T_5 = 706$ K and $P_5 = 1.0$ atm. Colors distinguish coordinate directions; line and marker styles identify the video from which measurements were obtained.

Two potential sources of axial (Z-direction) velocity in the unburned gas are evaluated analytically from the collected pressure data. The first, referred to here as residual, region-5 velocity ($u_{5,\mathrm{res}}$) takes into account the distance of the measurement location from the end wall and is calculated using measured attenuation rates of the incident and reflected shocks. Figure 3 shows extraction of the shock passage from PCB data and the results of applying a linear fit to the differential velocities for the same experiment reported in Fig. 2. A velocity offset is applied to the measured reflected-shock velocity (V_{rs}) to match the end-wall velocity necessary to stagnate the flow. Such a correction is justified as accounting for the growth rate of the reflected-shock bifurcation and will be evaluated in detail in a forthcoming, comprehensive work.

To obtain the state of the gas that is re-shocked at the measurement plane (L_5) at the time of the reflected shock, a particle tracking argument is required to determine the position L_1 at which the gas experienced the incident shock, which is found to be $L_1 = L_5(\rho_5/\rho_1)$, where the density ratio ρ_5/ρ_1 is well approximated by a nominal, end-wall solution to the reflected-shock equations. The state of the gas at the measurement plane is then found by successively applying the shock-jump equations using first the incident shock velocity at L_1 (i.e. $V_{is}(L_1)$) and secondly $V_{rs}(L_5)$; calculations were performed with a modified version of the in-house FROSH code to account for vibrational relaxation of the gas across the shocks [6].

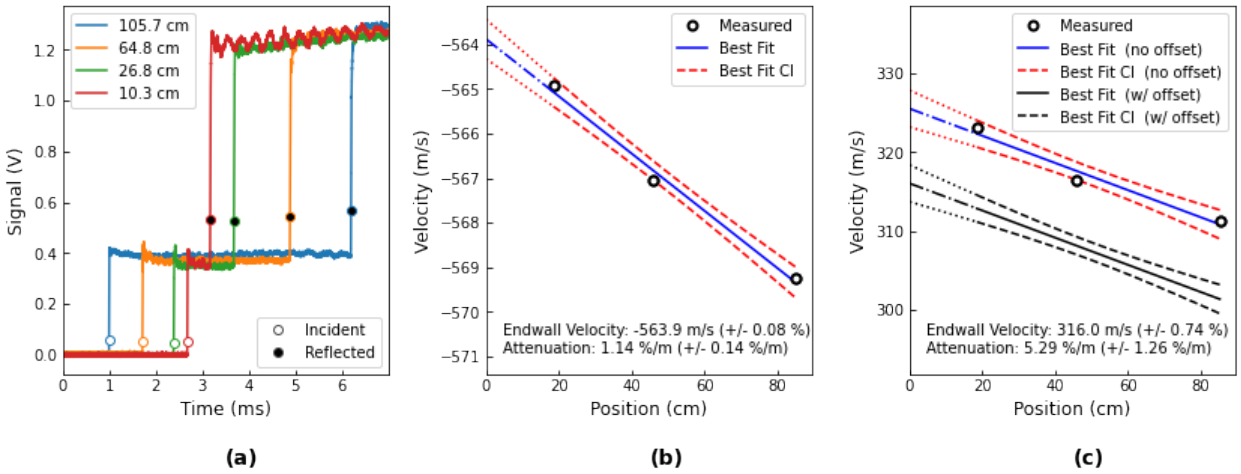

Figure 3: Example shock-experiment data showing a) identification of incident and reflected shocks from PCB data, b) differential velocity measurements and fit of incident-shock speed, and c) fit of reflected-shock velocity measurements, showing the offset applied to enforce zero-velocity at the end-wall.

The rate of post-reflected-shock pressure change ($\mathrm{d}P/\mathrm{d}t$) presents a second source of axial velocity that can be estimated from the available data. By considering the gas behind the reflected shock to be a cylinder of constant area, A, fixed at one end and undergoing isentropic compression, a relation can be drawn between the change in cylinder length (L) and the pressure, P:

$$\frac{P}{P_0} = \left(\frac{V_0}{V}\right)^{\gamma} = \left(\frac{A * L_0}{A * L}\right)^{\gamma} = \left(\frac{L_0}{L}\right)^{\gamma} \tag{1}$$

or, in a more convenient differential form:

$$\frac{\mathrm{d}L}{\mathrm{d}t} = \frac{-L}{\gamma}\frac{\mathrm{d}P}{P\mathrm{d}t} \equiv u_{\mathrm{d}P} \tag{2}$$

where $L = L_5$ is the location at which the velocity is evaluated, $\gamma = \gamma_5$ is the ratio of specific heats, and $u_{\mathrm{d}P}$ is the average velocity associated with an isentropic change in pressure at location L_5. The average rate of pressure change over a time interval is taken as the slope of a line fit to the Kistler pressure data, providing an estimate of of $u_{\mathrm{d}P}$ over that interval through Eqn. 2. In this work, the pressure data over the entire interval from the time of reflected-shock passage to that corresponding with the last frame used in the velocimetry measurement is used to evaluate $\mathrm{d}P/\mathrm{d}t$ and $u_{\mathrm{d}P}$.

3. Results and Discussion

3.1 Post-Shock Gas Velocity

Measurements of the 3-dimensional (3D) core gas velocity were performed behind reflected shocks across 24 experiments using FDV, results of which are presented in Fig. 4. Propane and *n*-heptane are used as fuels, prepared at lean equivalence ratios ($0.3 \leq \phi \leq 0.9$) with oxidizer mixtures consisting of 18.0% to 21.4% O_2 with various combinations N_2, Ar, and He comprising the diluent(s).

Post-reflected-shock temperatures computed at the measurement plane fall in the range 560 K $\leq T_5 \leq$ 1,035 K and pressures are near atmospheric (0.9 atm $\leq P_5 \leq$ 1.2 atm). Relatively short spark delay times in the range 0.3 ms $\leq t_{\text{spark}} \leq$ 1.7 ms were used for the reported measurements, and reported velocities are based on the first 250 μs (6 frames) of video after the spark.

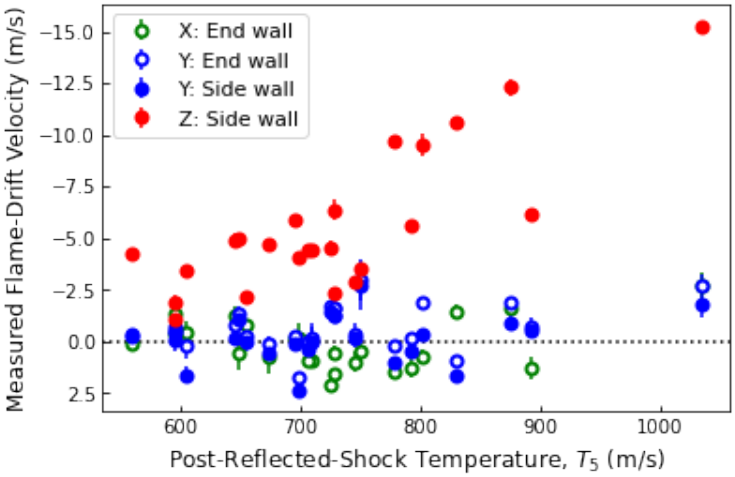

Figure 4: Velocimetry results obtained from the end-wall

Across all measurements, the X and Y components of the velocity are found to be small in magnitude ($\leq$ 3 m/s), and show no clear trend with temperature. The average, measured X and Y velocities are 0.2 m/s and -0.4 m/s, respectively. Comparing Y velocities obtained from the side- and end-wall perspectives provides a means of estimating the uncertainty of the FDV measurements; the average absolute difference is 0.52 m/s, which is comparable to the linear-fit slope uncertainties (error bars in Fig. 4) that average 0.35 m/s for the Y-component velocities.

The Z (axial) velocity component shows both a larger magnitude than the X and Y components and a clear trend with temperature, increasing in magnitude with T_5; per the coordinates defined in Fig. 1, negative Z velocities indicate motion towards the driven end wall. These measured velocities are compared to $u_{5,\text{res}}$ calculated from measured shock-attenuation rates and u_{dP} estimated from the pressure-time histories; Fig. 5 displays the calculated vs. measured axial (Z) velocity values, with calculated $u_{5,\text{res}}$ and u_{dP} plotted independently as open circles (red and blue, respectively) and summed as black, filled circles. Linear fits of each calculated dataset are shown as dashed lines of corresponding color; the dotted line is a reference of unity slope.

It is apparent from Fig. 5 that, while neither $u_{5,\text{res}}$ nor u_{dP} are predictive of the measured post-reflected-shock velocity by themselves, together they can accurately predict the core-gas velocity; the best-fit line of the combined, calculated velocity coincides almost perfectly with the unity-slope reference line. This observation suggests that the residual velocity associated with the attenuation of the incident and reflected shocks is independent of the area-averaged compression associated with post-shock dP/dt. An implication of this observation is that $u_{5,\text{res}}$, being the larger velocity component as seen in Fig. 5, cannot be eliminated by controlling dP/dt alone, as is often done in shock tube experiments with driver inserts [20]. As such, some amount of axial motion in the core gas might be considered as inherent to shock tube experiments.

It is further noted that both $u_{5,\text{res}}$ and u_{dP} exhibit direct proportionality to the axial position L_5 at which a measurement is performed, implying that the magnitude of the core-gas velocity would

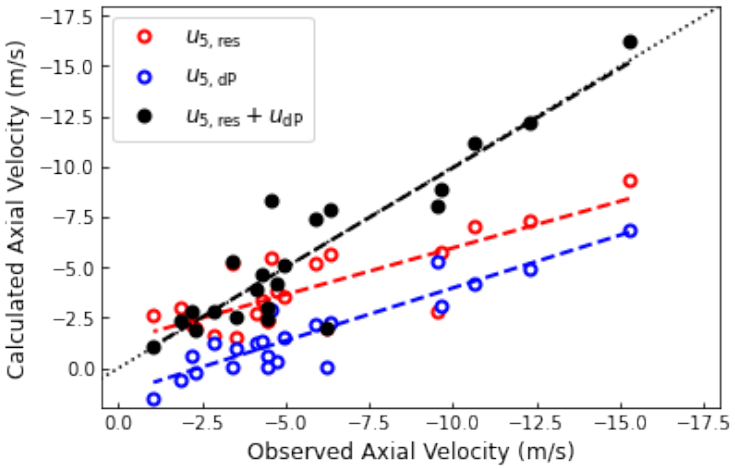

Figure 5: Calculated vs. observed axial (Z-direction) gas velocity. Two velocity models ($u_{5,\mathrm{res}}$ and u_{dP}) are shown independently as red and blue symbols, respectively, and summed as black symbols. Dashed lines are fits to data of the corresponding color.

be expected to be much lower (by a factor of 5-10) at the 1-2 cm locations at which shock-tube measurements are typically performed [4] than the 10-cm plane in which the FDV measurements reported here are performed. As such, while the quiescent-gas assumption might be considered to be reaffirmed by these measurements as it relates to traditional chemical kinetics experiments, objectionable axial gas velocities might be expected to affect flames ignited at large distances L_5 from the end wall and at high T_5 values. This finding motivates that future works employing the shock-tube flame speed method should seek to minimize the axial distance of the measurement plane, to the extent possible, in order to reduce the prevalence of non-ideal flows. Recent flame speed measurements performed at the 2-cm measurement plane at T_{u} up to nearly 1,200 K demonstrate the merit of this experimental refinement [21].

3.2 Flame Morphology

Dual-perspective imaging additionally provides the first opportunity to fully evaluate the morphology of flames ignited in the post-reflected-shock environment. Figure 6 shows a comparison of select end- and side-wall images for experiments performed at three different values T_5; lean *n*-heptane (φ= 0.9) in an oxidizer of 18% O_2, 41% He, and 41% Ar is used in all three experiments, matching the fuel-air mixture used in a previous work reporting flame structure [13]. End-wall images (left column) are scaled and cropped to match the resolution and FOV of the side-wall images (right column). In side-wall images, the driven-section end wall is to the left, such that the bulk motion of the flames is in the negative-Z direction, towards the end wall.

For all three flames shown in Fig. 6, the initial flame kernels (top row) appear the same in the end- and side-wall images, indicating that the expected axis-symmetric ignition-kernel structure is realized in all cases. However, while the flame at the lowest unburned-gas temperature (T_5 = 646 K, Fig. 6a) maintains its symmetric appearance throughout its growth, the higher-temperature flames (Fig. 6b-c) notably distort as they propagate. The flame shown in Fig. 6b, in particular, develops a highly irregular shape as viewed from the side, the axial integration of which leads to

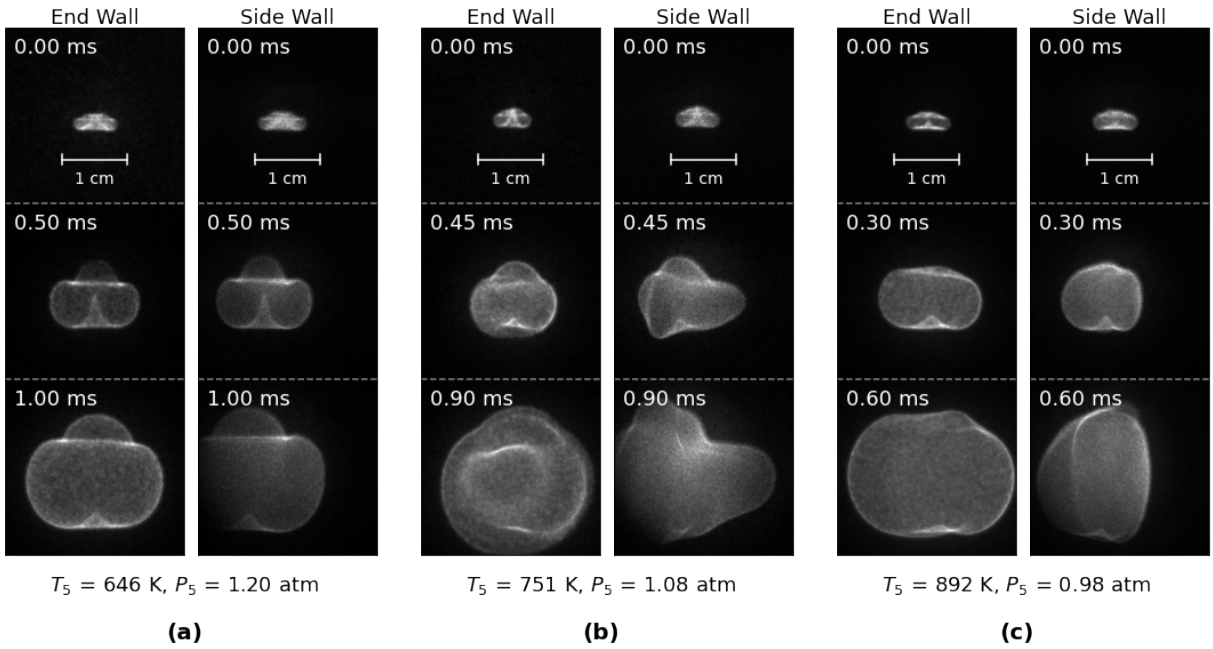

Figure 6: Select frames comparing the flame morphology as seen in end- and side-wall images. a) Axis-symmetry flame at T_5 = 646 K, b) highly distorted flame at T_5 = 751 K, and c) axially compressed flame at T_5 = 892 K.

an inner, bright ring in the end-wall view, consistent with the structure reported in previous studies of *n*-heptane and *iso*-octane flames at comparable temperatures [12, 13]. Figure 6c, the highest T_5 shown, simultaneously displays horizontal (X-direction) stretching in the end-wall view and axial (Z-direction) compression viewed from the side. This observed distortion demonstrates the utility of dual-perspective imaging in characterizing flame morphology, which should be employed in future works seeking to reliably measure flame speeds in a shock-tube environment.

4. Conclusions

Measurements of the core-gas velocity behind reflected shocks are reported using 3D FDV and dual-perspective imaging. While X and Y (radial) velocities are found to be small in magnitude and random, the Z (axial) velocity is larger, always manifests in the direction of the driven end wall, and displays notable temperature dependence. Calculated axial velocities, $u_{5,\mathrm{res}}$ based on measured shock speeds and attenuation rates and u_{dP} based on post-shock pressure change, are shown to accurately describe the measured velocities when combined, suggesting the effects are independent. The functional, direct dependence of both sources of axial velocity on the measurement position, L_5, provides guidance to future experiments on a pathway to reduce the non-ideal velocity effects by moving the measurement location closer to the driven end wall.

Dual-perspective imaging also provides the first opportunity to evaluate the 3D morphology of flames in the shock-tube environment. While the previously assumed axis-symmetric structure is confirmed at a comparably low T_5 = 646 K, flames at higher temperature exhibit axial distortion not apparent from the end-wall images alone. The observed distortion provides a new understanding that previously reported concentric flame structure [12, 13] likely results from end-wall images ax-

ially integrating emission from distorted flames. The cause of the axial distortion, whether caused purely by an underlying flow field or the result of localized double-flame formation [22], requires further study. Both the FDV measurements and morphology characterization reported here demonstrate the value brought by the addition of side-wall imaging to shock-tube flame experiments, providing new insights and guidance towards the optimization of future high-temperature flame investigations.

5. Acknowledgments

This work was supported by the National Science Foundation under award number 1940865, contract monitors Dr. Harsha Chelliah (former) and Dr. John Daily (current). A. J. Susa recognizes the U.S. Department of Defense for financial support through a NDSEG Fellowship. Additional thanks is provided to LaVision for providing the demonstration HS-IRO-X unit used in this work.

References

[1] W. Shepherd, The Ignition of gas mixtures by impulsive pressures, Symposium on Combustion and Flame, and Explosion Phenomena (1948), pp. 301–316, DOI: 10.1016/S1062-2896(49)80037-7.

[2] S. Bauer, Chemical kinetics in shock tubes, Science 141 (1963) 867–879. DOI: 10.1126/science.141.3584.867.

[3] W. Tsang and A. Lifshitz, Shock tube techniques in chemical kinetics, Annual review of physical chemistry 41 (1990) 559–599. DOI: 10.1146/annurev.pc.41.100190.003015.

[4] R. K. Hanson and D. F. Davidson, Recent advances in laser absorption and shock tube methods for studies of combustion chemistry, Progress in Energy and Combustion Science 44 (2014) 103–114. DOI: 10.1016/j.pecs.2014.05.001.

[5] A. M. Ferris, A. J. Susa, D. F. Davidson, and R. K. Hanson, High-temperature laminar flame speed measurements in a shock tube, Combust. Flame 205 (2019) 241–252. DOI: 10.1016/j.combustflame.2019.04.007.

[6] M. F. Campbell, K. G. Owen, D. F. Davidson, and R. K. Hanson, Dependence of calculated postshock thermodynamic variables on vibrational equilibrium and input uncertainty, Journal of Thermophysics and Heat Transfer 31 (2017) 586–608. DOI: 10.2514/1.T4952.

[7] H. Mark, The interaction of a reflected shock wave with the boundary layer in a shock tube, National Advisory Committee for Aeronautics, 1958.

[8] M. Kono, K. Niu, T. Tsukamoto, and Y. Ujiie, Mechanism of flame kernel formation produced by short duration sparks, Symposium (International) on Combustion (1989), pp. 1643–1649, DOI: 10.1016/S0082-0784(89)80176-6.

[9] T. Spiglanin, A. Mcilroy, E. Fournier, R. Cohen, and J. Syage, Time-resolved imaging of flame kernels: laser spark ignition of H2/O2/Ar mixtures, Combustion and Flame 102 (1995) 310–328. DOI: 10.1016/0010-2180(94)00278-Z.

[10] D. Bradley, C. Sheppard, I. Suardjaja, and R. Woolley, Fundamentals of high-energy spark ignition with lasers, Combustion and Flame 138 (2004) 55–77. DOI: 10.1016/j.combustflame.2004.04.002.

[11] T. X. Phuoc, Laser-induced spark ignition fundamental and applications, Optics and Lasers in Engineering 44 (2006) 351–397. DOI: 10.1016/j.optlaseng.2005.03.008.

[12] A. J. Susa, A. M. Ferris, D. F. Davidson, and R. K. Hanson, Experimental observation of negative temperature dependence in iso-Octane burning velocities, AIAA Journal 57 (2019) 4476–4481. DOI: 10.2514/1.J058530.

[13] A. J. Susa, A. M. Ferris, D. F. Davidson, and R. K. Hanson, Experimental measurement of laminar burning velocity of n-heptane at variable extents of reactions in a shock tube, Int. Symp. on Shock Waves 32 (2019), DOI: 10.3850/978-981-11-2730-4_0149-cd.

[14] Z. Shi, Local air-fuel ratio and gas velocity measurements in flames using LIBS, PhD thesis, Imperial College London, 2018.

[15] Z. Shi, Y. Hardalupas, and A. M. Taylor, Laser-induced plasma image velocimetry, Experiments in Fluids 60 (2019) 1–13. DOI: 10.1007/s00348-018-2649-2.

[16] V. Troutman, C. Strand, M. Campbell, A. Tulgestke, V. Miller, D. Davidson, and R. Hanson, High-speed OH* chemiluminescence imaging of ignition through a shock tube end-wall, Applied Physics B 122 (2016) 56. DOI: 10.1007/s00340-016-6326-y.

[17] N. Otsu, A threshold selection method from gray-level histograms, IEEE transactions on systems, man, and cybernetics 9 (1979) 62–66. DOI: 10.1109/TSMC.1979.4310076.

[18] S. van der Walt, J. L. Schönberger, J. Nunez-Iglesias, F. Boulogne, J. D. Warner, N. Yager, E. Gouillart, T. Yu, and the scikit-image contributors, scikit-image: image processing in Python, PeerJ 2 (2014) e453. DOI: 10.7717/peerj.453.

[19] P. Virtanen et al., SciPy 1.0: Fundamental Algorithms for Scientific Computing in Python, Nature Methods 17 (2020) 261–272. DOI: 10.1038/s41592-019-0686-2.

[20] Z. Hong, G. A. Pang, S. S. Vasu, D. F. Davidson, and R. K. Hanson, The use of driver inserts to reduce non-ideal pressure variations behind reflected shock waves, Shock Waves 19 (2009) 113–123. DOI: 10.1007/s00193-009-0205-y.

[21] A. J. Susa, L. Zheng, and R. K. Hanson, Schlieren-based measurements of propane flame speeds at extreme temperatures, In 12th US National Combustion Meeting (2021).

[22] T. Zhang, A. J. Susa, R. K. Hanson, and Y. Ju, Multiscale modeling of spherical double flame formation induced by the laser ignition under shock-tube conditions, In 12th US National Combustion Meeting (2021).